Alma Mater Studiorum Università di Bologna
Archivio istituzionale della ricerca

On the LoRa Chirp Spread Spectrum Modulation: Signal Properties and Their Impact on Transmitter and Receiver Architectures

(Article begins on next page)

01 January 2025

On the LoRa chirp spread spectrum modulation. Signal properties and their impact on transmitter and receiver architectures.

Gianni Pasolini, *Member, IEEE*

The LoRa modulation scheme is arousing a growing interest in the Internet of Things community as it is adopted by the emerging LoRaWAN technology. In this paper, we firstly analyse the baseband processing for the generation of LoRa signals at the transmitter side, providing a simple algorithm that leverages digital signal processing techniques to reduce the modulator complexity. Secondly, we analytically investigate the signal demodulation technique. Quite surprisingly, we found that its effectiveness depends on the particular choice of the sampling frequency at the receiver side, which purposely does not meet the sampling theorem requirement. Finally, we consider the actual architecture of digital receivers investigating the trade-off between the selectivity of receive digital filters, which impacts on the required computational effort and power consumption, and the receiver performance.

I. INTRODUCTION

THE term Internet of Things (IoT) was first used in 1999 to describe a scenario where the Internet is connected to the physical world via ubiquitous sensors [1]. Two decades on, a lot of progress has been made in this direction, as several communication technologies, both short- and long-range, have been developed, which are capable of supporting IoT applications in different contexts and environments.

Focusing the attention on long-range technologies, Low-Power Wide-Area Networks (LPWANs) have recently appeared on the IoT stage [2], the most popular being Lo-RaWAN, SigFox, and NB-IoT [3]. Such networks are peculiar in that they combine wide coverage (even several kms) and long battery life (even ten years), at the cost of a low bit rate.

At the time of writing, LoRaWAN represents the "de-facto" standard for the Internet of Things, being installed in 163 countries by 150 network operators [4] to enable a wide range of services [5]–[8]. With more than 170 million of already connected devices [9], and with the expectation that more than 50% of all non-cellular LPWAN connections will be LoRa-enabled by 2026, this technology is predicted to dominate the LPWANs market in the next years.

From a technical point of view, LoRaWANs are defined by an open standard [10] developed by the LoRa Alliance, which mainly defines the Medium Access Control (MAC)

layer and the message formats. At the physical (PHY) layer, they are based on LoRa, a proprietary modulation scheme developed by Semtech Corporation and derived from Chirp Spread-Spectrum (CSS).

In the following sections, we provide an in-depth analysis of the LoRa PHY layer. We start by investigating the generation of the modulated signal at the transmitter, which is addressed leveraging digital signal processing techniques. We also focus the attention on the receiver, providing a frequency-domain analysis of the demodulation technique. Although the numerical demodulation algorithm adopted by LoRa receivers is well-known, since it is described in [11], [12] and discussed in several excellent papers, such as [13], [14], no paper has dealt so far with the frequency-domain implications of each of its steps, which however reveal the brilliant idea behind its remarkable performance.

Finally, we also investigate the receiver performance as a function of the signal-to-noise ratio. This topic is covered by many papers, such as [15]–[19]. However, all of them assume ideal filtering at the receiver side, which may be impossible to implement, due to constraints on the available computational power or the need to reduce the energy consumption. In this paper, we consider the real architecture of modern receivers, which usually include digital filters, and we investigate the impact of the filters' selectivity on the receiver performance.

The main contributions of this paper can be summarized as follows:

- we provide an original strategy for the generation of LoRa signals, which leverages digital signal processing techniques to reduce the transmitter complexity (Sec.IV),
- we analytically investigate the demodulation technique described in the patent documents [11], [12] filed by Semtech, revealing still unknown aspects, mainly concerning the impact of signal undersampling, that are the key elements for its effectiveness (Sec.V),
- we investigate the trade-off between the receiver performance and the complexity of digital receive filters, which impacts on the energy consumption and the required computational effort (Sec.VI).

Notation. Throughout this paper, we define the indicator function $g_T(t) = 1$ for $0 \leq t < T$ and $g_T(t) = 0$ elsewhere and we denote by j the imaginary unit. For the reader's convenience, in Table I we reported the main symbols introduced in the following, along with their meanings.

G. Pasolini is with the Department of Electrical, Electronic and Information Engineering "G. Marconi", University of Bologna, viale Risorgimento 2, 40136, Bologna, Italy and with the National Laboratory of Wireless Communications (WiLab) of CNIT. E-mail: gianni.pasolini@unibo.it.

TABLE I
TABLE OF SYMBOLS AND RELATED MEANINGS

Symbol	Meaning
f_s	Sampling frequency for signal generation (Tx side)
$f_s^{(d)}$	Sampling frequency for signal demodulation (Rx side)
$f_s^{(ADC)}$	Sampling frequency adopted by the ADCs (Rx side)
n_s	Number of symbols in the payload
B	Width of the frequency sweep interval
D	Decimation factor
M	Modulation order
N	Number of samples in a symbol interval (Tx side)
SF	Spreading factor
$T = \frac{1}{f_s}$	Sampling interval (Tx side)
T_h	Time instant in which $\Delta f(s,t)$ wraps around
$T_{\hat{h}}$	Residual chirp duration after the folding of $\Delta f(s,t)$
T_s	Symbol time (*i.e.*, chirp duration)

II. ORIGINAL CONTRIBUTIONS WITH RESPECT TO THE EXISTING LITERATURE

LoRa signals have been investigated in several papers. Those that are most related to the content of this article are discussed below.

The generation of LoRa modulated chirps starting from the time-shift of a basic chirp was proposed in 2019 by Nguyen *et.al.* [20] and Elshabrawy *et.al.* [21], which are rightly credited with being the first to introduce numerical processing techniques to reduce the complexity of LoRa transmitters. However, the signal generated adopting the techniques presented in [20], [21] does not exhibit the continuous-phase property when passing from one symbol (i.e., one chirp) to the following one, which was demonstrated in the same year by Chiani *et.al* in [14]. The enhancement proposed by Elshabrawy *et.al.* in [22], while introducing phase continuity, generates a discrete-time signal with a sampling rate that might be critical for real implementations. This aspect will be discussed in Sec.IV, where an original expression of the sampled phase of LoRa chirps is provided.

The characteristics of LoRa signals, both in the time and frequency domains, have been instead investigated in [13] and [14], which also discuss the demodulation strategy. In [13], Vangelista gives the first mathematical description of the modulation and demodulation processes, providing the theoretical derivation of the optimum receiver based on the Fast Fourier Transform. The performance of the LoRa modulation is also derived both in an additive white Gaussian noise (AWGN) channel and in a frequency selective channel. In [14], Chiani *et.al* analysed the LoRa M-ary modulation, providing the signal description in the time domain and showing that LoRa is a memoryless continuous phase modulation. The cross-correlation between the transmitted waveforms is also derived in [14], proving that LoRa can be considered approximately an orthogonal modulation only for large M. Finally, in [14] the spectral characteristics of the signal modulated by random data is investigated, obtaining a closed-form expression of the spectrum in terms of Fresnel functions. Although very thorough and inspiring, the analyses provided in [13], [14] do not address the fundamental role played by undersampling and aliasing in the demodulation process, which is instead the original contribution reported in

Sec.V of this paper.

Regarding the performance of the LoRa modulation, many papers present analytical or simulative investigations. In [15] and [16], for instance, the symbol error rate (that is, the chirp error rate) is derived as a function of the signal-to-noise ratio. In [17], the closed-form expression of the bit error probability is derived in AWGN and Rayleigh channels. Similar results are presented in [18], [19], [23] for different signal parameters, channel conditions and demodulation techniques. However, none of the papers in the literature consider the trade-off between the performance and the complexity of the digital filters implemented in LoRa receivers, which is instead addressed in Sec.VI of this paper.

The analysis of the LoRa physical layer reported in the above referenced articles and in this manuscript would not be complete without mentioning the impact of interference and capture effect on the receiver performance. These topics are out of the scope of this document, mainly because they have been specifically addressed by many papers. In [24] the interference between LoRa signals is analysed for different spreading factors and bandwidths, whereas in [25], [26] the use of successive interference cancellation is considered to decode superposed LoRa signals. The capture effect is experimentally investigated in [27], [28] and analytically investigated in [26], [29], [30]. Both analysis and simulations are instead discussed in [15], [31].

III. LORA SIGNAL

LoRa is a proprietary spread-spectrum modulation scheme patented by Semtech Corporation [32], which is derivative of CSS. In general, a sine-wave chirp signal, concisely denoted as *chirp* in the following, consists of a short-time frequency sweep mathematically expressed as

$$c(t) = V_0 \cos\left(2\pi \int_{t_0}^{t} f(\xi)d\xi + \phi_0\right), \quad t_0 \leq t \leq t_0 + T_c \quad (1)$$

where

- $V_0 > 0$ is the chirp amplitude,
- $f(t)$ is the instantaneous frequency,
- ϕ_0 is the signal phase at the initial instant t_0,
- T_c is the chirp duration.

Denoting with f_0 the central frequency of the sweep interval $[f_0 - \frac{B}{2}, f_0 + \frac{B}{2}]$ and assuming, without loss of generality, $t_0 = 0$ and $\phi_0 = 0$, (1) can also be written as

$$c(t) = V_0 \cos\left(2\pi f_0 t + 2\pi \int_{0}^{t} \Delta f(\xi)d\xi\right), \quad 0 \leq t \leq T_c \quad (2)$$

with $\Delta f(t)$ representing the instantaneous frequency-offset, ranging in the interval $[-\frac{B}{2}, \frac{B}{2}]$, with respect to f_0.

Equation (2) is the basis of the LoRa modulation, which uses M differently shaped chirps, each of which is in one-to-one correspondence with the M symbols of the modulation alphabet $\mathcal{S} = \{0, \cdots, M-1\}$. In particular, given a modulation symbol $s \in \mathcal{S}$, the instantaneous frequency-offset $\Delta f(s,t)$ of the corresponding modulated chirp linearly increases starting from $-\frac{B}{2} + \frac{B}{M}s$. Then, when the maximum frequency-offset $\frac{B}{2}$ is reached, $\Delta f(s,t)$ wraps around to $-\frac{B}{2}$ and keeps on
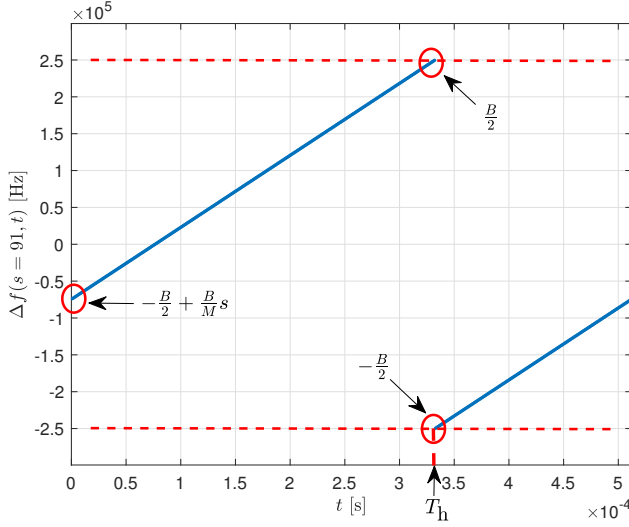
Fig. 1. Instantaneous frequency-offset. $s = 91$, SF=8, $B = 500$ kHz, $T_s = \frac{2^{\text{SF}}}{B} = 5.12 \cdot 10^{-4}$s.

increasing linearly. Assuming $t_0 = 0$ as the symbol starting instant, the chirp stops when $\Delta f(s, t = T_s) = \Delta f(s, 0)$. Its duration T_s is usually referred to as *symbol time*.

In mathematical terms, still considering the symbol interval $[0, T_s]$, for any given modulation symbol s it is:

$$\Delta f(s,t) = \begin{cases} -\frac{B}{2} + \frac{B}{M}s + \frac{B}{T_s}t, & 0 \leq t < T_{\text{h}}, \\ -\frac{3B}{2} + \frac{B}{M}s + \frac{B}{T_s}t, & T_{\text{h}} \leq t \leq T_s \end{cases} \quad (3)$$

with $T_{\text{h}} = T_s - \frac{T_s}{M}s$ denoting the time instant in which $\Delta f(s, t)$, having reached $\frac{B}{2}$, wraps around to $-\frac{B}{2}$.

In the specific case of LoRa, the modulation parameters are chosen such that

- $B \in \{125, 250, 500\}$ kHz,
- $M = 2^{\text{SF}}$, with SF denoting the *spreading factor*,
- SF $\in \{7, 8, 9, 10, 11, 12\}$,
- $BT_s = M$.

In Fig.1, an example of instantaneous frequency-offset with $s = 91$, $B = 500$ kHz and SF=8 is given: one observes that $\Delta f(s = 91, t)$ linearly sweeps within the interval $[-\frac{B}{2}, \frac{B}{2}]$ and wraps around at $T_{\text{h}} = 3.3 \cdot 10^{-4}$s.

According to [33], [34], a specific frame format is used at the physical layer of Semtech devices to accommodate data: A LoRa frame begins with a preamble, that consists of a configurable number of pure upchirps, whose frequency-offset linearly increases from $-\frac{B}{2}$ to $\frac{B}{2}$ (see Fig.2(a) for the frequency-offset of a pure upchirp in the case SF=12 and $B = 500$ kHz), followed by two and a quarter downchirps, and, optionally, a frame header. The remainder of the frame includes the payload, which carries n_s symbols, and, optionally, the corresponding CRC.

Focusing on the payload, one observes that it consists of a sequence of n_s modulated chirps, each of which with an instantaneous frequency-offset similar to the one depicted in Fig.1 (they differ each other by the "wraps around instant" T_{h}, which depends on s). In this regard, one observes that,

irrespectively of the modulation symbol s, it is[1]

$$\int_0^{T_s} \Delta f(s, \xi)d\xi = 0. \quad (4)$$

This means that the phase term

$$\theta(s, t) = 2\pi \int_0^t \Delta f(s, \xi)d\xi \quad (5)$$

in (2) is such that

$$\theta(s, T_s) = \theta(s, 0) = 0. \quad (6)$$

The proof is reported in Appendix A.

Equation (6) immediately results in the following two properties:

- *Property 1:* The LoRa signal exhibits continuous phase when passing from one modulation symbol to the following one. In particular, the phase at the beginning and at the end of each symbol interval is equal to zero.
- *Property 2:* In any given symbol interval, irrespectively on the symbol s to be transmitted, the shape of the modulated chirp does not depend on the previously transmitted symbols, as the initial and final phases in a symbol interval are coincident.

The above properties, which were first derived in [14] (albeit in a different way), imply that LoRa is a memoryless continuous phase modulation. *Properties* 1 and 2 are here recalled because they are particularly useful from a practical point of view, as they ease the generation of the modulated signal at the transmitter side. This aspect is discussed in the following section.

IV. LoRa SIGNAL GENERATION

Since the waveform transmitted in each symbol interval depends only on the symbol to be transmitted in that interval (*Property 2*), the generation of LoRa signals boils down to the generation of a sequence of independently modulated chirps, each of which starting and ending with the phase term equal to zero (*Property 1*). In particular, denoting with $\Delta f(s^{(n)}, t)$ the instantaneous frequency-offset related to the symbol $s^{(n)}$ in the time interval $[nT_s, (n + 1)T_s]$, and with $\theta(s^{(n)}, t)$ the corresponding phase term, the modulated chirp to be transmitted in the same interval is

$$c_n(t) = V_0 \cos\left(2\pi f_0 t + 2\pi \int_{nT_s}^t \Delta f(s^{(n)}, \xi)d\xi\right)$$
$$= V_0 \cos\left(2\pi f_0 t + \theta(s^{(n)}, t)\right) \quad (7)$$

with $n = 0, 1, \ldots, n_s - 1$, and $nT_s \leq t \leq (n + 1)T_s$.

The corresponding complex envelope in the same symbol interval is thus

$$i_n(t) = V_0 e^{j\theta(s^{(n)}, t)}. \quad (8)$$

---

[1]The proof, based on geometric reasoning, is trivial and is omitted for the sake of conciseness.
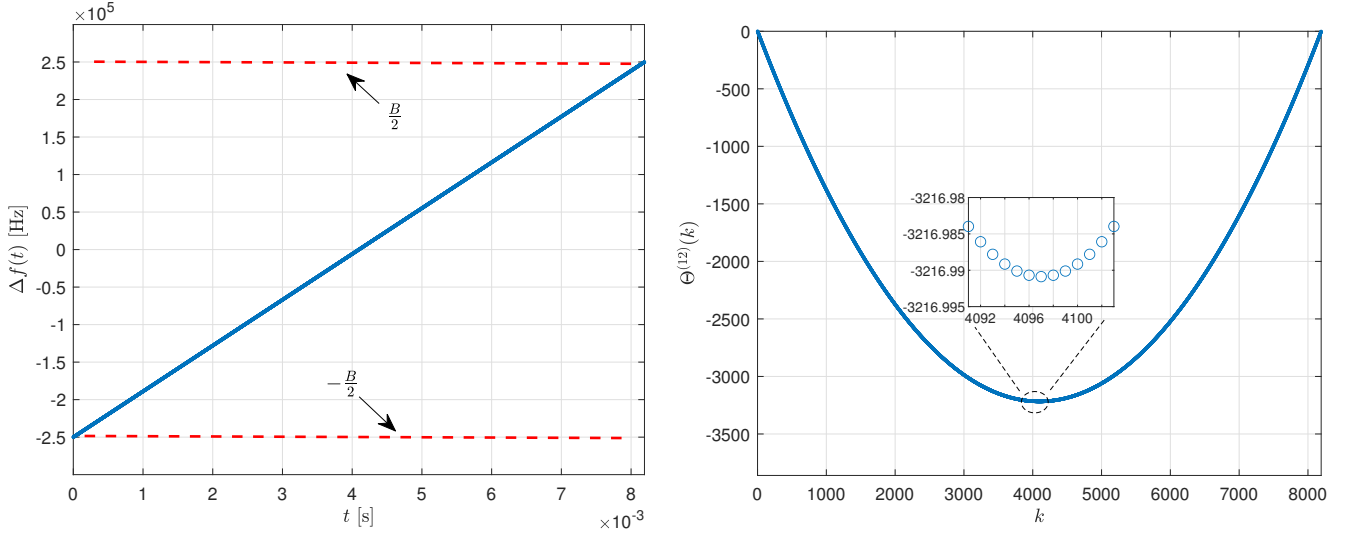
(a) Pure upchirp: instantaneous frequency-offset. SF=12, $B = 500$ kHz, $T_s = 8.2 \cdot 10^{-3}$ s.

(b) Reference upchirp phase. Some of the $2M = 8192$ samples are shown in details in the zoomed box.

Fig. 2. Instantaneous frequency-offset and phase of a pure upchirp. SF=12, $B = 500$ kHz.
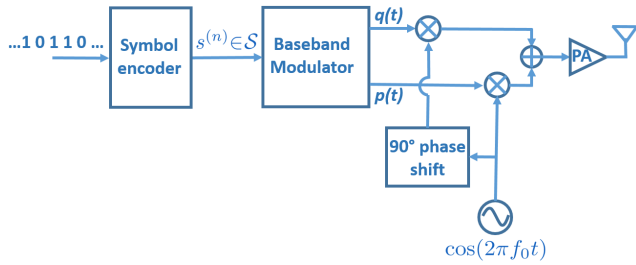

Fig. 3. Transmitter: Quadrature modulator architecture. The triangle labelled "PA" represents the power amplifier.

Given (8), due to the memoryless nature of the modulation, the complex envelope of the LoRa signal[2] can be written as

$$i(t) = V_0 \sum_{n=0}^{n_s-1} e^{j\theta(s^{(n)}, t)} g_{T_s}(t - nT_s). \qquad (9)$$

As shown also in the block diagram reported in the LoRa patent application EP2763321A1 [11], transmitters usually adopt a quadrature modulator architecture (see Fig.3), which requires the generation of the in-phase and quadrature base-band signals $p(t) = \Re\{i(t)\}$ and $q(t) = \Im\{i(t)\}$:

$$p(t) = V_0 \sum_{n=0}^{n_s-1} \cos\left(\theta(s^{(n)}, t)\right) g_{T_s}(t - nT_s) \qquad (10)$$

$$q(t) = V_0 \sum_{n=0}^{n_s-1} \sin\left(\theta(s^{(n)}, t)\right) g_{T_s}(t - nT_s). \qquad (11)$$

In the perspective of a digital implementation, this means that the baseband stage of the transmitter needs to generate

the discrete-time signals

$$p(kT) = V_0 \sum_{n=0}^{n_s-1} \cos\left(\theta(s^{(n)}, kT)\right) g_{T_s}(kT - nT_s) \qquad (12)$$

$$q(kT) = V_0 \sum_{n=0}^{n_s-1} \sin\left(\theta(s^{(n)}, kT)\right) g_{T_s}(kT - nT_s), \qquad (13)$$

with $k \in \mathbb{Z}$ and T denoting a properly chosen sampling interval. These signals are then converted from digital to analog in the final stage of the baseband modulator, which includes a pair of digital-to-analog converters (DACs)[3] for the generation of (10) and (11)[4].

Clearly, the sampling frequency $f_s = \frac{1}{T}$ must be such that the Shannon-Hartley sampling theorem is fulfilled with reference to $p(t)$ and $q(t)$, whose generation technique is the final objective of the present section. In this regard, it is worth stressing that having the instantaneous frequency sweeping over B does not imply that the bandwidth of the radiofrequency (RF) signal is B. In particular, Chiani *et al.* in [14] (Table I) show that the largest bandwidth occupation (*i.e.*, the worst case for the sampling theorem) occurs when SF=7. In such a case, it is $B_{99} = 1.045B$, with B_{99} denoting the RF bandwidth centred on f_0 containing 99% of the power.

Since the discussion herein considers the baseband components $p(t)$ and $q(t)$ of LoRa RF signals, one should assume a bandwidth occupation of $p(t)$ and $q(t)$ equal to $\frac{B_{99}}{2}$. It follows that f_s should be such that $f_s \geq 2\frac{B_{99}}{2}$, that is, in the worst case, $f_s \geq 1.045B$. As shown hereafter, a convenient choice is $f_s = 2B$, which largely fulfils the sampling theorem requirement.

---

[2]Here, we do not consider the preamble, which does not depend on modulation symbols.

[3]The DACs are not shown in Fig.3, as they are inside the Baseband Modulator block.

[4]Alternatively, the sampled in-phase and quadrature waveforms might be multiplied by the sampled in-phase and quadrature sinusoids, summed up and then digital-to-analog converted. This solution is not reflected in Fig.3.

One might observe that $B_{99} \simeq B$, so that the bandwidth of $p(t)$ and $q(t)$ can be assumed equal to $\frac{B}{2}$ without a significant lack of accuracy. Although this is certainly true, it does not mean that choosing $f_s = B$ is a reasonable choice, as it would appear by simply considering the sampling theorem condition. In fact, when it comes to actually implement the transmitter with digital processing techniques, one has to consider that any DAC includes an analog low-pass filter, aimed at preserving undistorted the spectrum in the frequency interval $[-\frac{B}{2} \frac{B}{2}]$ and removing the periodic spectral replicas that occur with period f_s. Choosing $f_s = B$ would mean that the spectral replicas are perfectly adjacent (actually, there might even be a little overlap at their boundaries for low SFs), thus leaving no room for the DAC's filter to completely remove the spectral components in the immediate vicinity of the interval $[-\frac{B}{2} \frac{B}{2}]$.

The remainder of this section is aimed at showing how the baseband modulator of a LoRa digital transmitter can generate the baseband discrete-time signals (12) and (13) with $f_s = 2B$.

A. Step 1: Generation of the reference phase term

One considers, firstly, a pure upchirp, whose instantaneous frequency-offset $\Delta f(t)$ linearly increases from $-\frac{B}{2}$ to $\frac{B}{2}$. Fig.2(a) shows an example of pure upchirp in the case $B = 500$ kHz and SF=12. The analytical expression of the corresponding phase term $\theta(t) = 2\pi \int_0^t \Delta f(\xi)d\xi$ in the symbol interval $[0, T_s]$ can be easily derived:

$$\theta(t) = 2\pi \left[-\frac{B}{2}t + \frac{B}{2T_s}t^2 \right], \quad 0 \le t \le T_s. \tag{14}$$

Since (14) refers to a pure upchirp, in the following it will be denoted as *upchirp phase*. One considers, now, the discrete-time upchirp phase

$$\left\{ \theta(k) \right\}_{k=0}^{N-1} = \theta(0), \theta(T), \ldots, \theta\big((N-1)T\big) \tag{15}$$

obtained taking N uniformly spaced samples of (14) in a symbol interval. Assuming $T = \frac{1}{f_s} = \frac{1}{2B}$, as previously stated, it results

$$\left\{ \theta^{(\mathrm{SF})}(k) \right\}_{k=0}^{N-1} = \left\{ k\frac{\pi}{2} \left[-1 + \frac{k}{2^{\mathrm{SF}+1}} \right] \right\}_{k=0}^{N-1}. \tag{16}$$

The proof of (16) is reported in Appendix B.

Remark 1. One observes that (14) depends on the parameters B and T_s. Given the relationship $BT_s = 2^{\mathrm{SF}}$ that holds for LoRa signals, it clearly appears that $\theta(t)$ depends, ultimately, on two of the three parameters B, T_s and SF. In (16), the dependence on SF appears explicitly in the right-hand term, whereas the dependence on B is implicitly taken into account by the time interval $T = \frac{1}{2B}$ between two consecutive samples. For the sake of conciseness, in the left-hand term of (16) we explicitly highlighted in the superscript only the dependence on SF, which is the key parameter for the following discussion.

Having chosen $f_s = 2B$, and recalling that $BT_s = M$, it results $N = f_s T_s = 2M$, that is, $N = 2^{\mathrm{SF}+1}$. As it is evident, N increases for increasing values of SF, reaching its maximum $N_{\max} = 8192$ for SF=12.

In the following, we show that starting from the $N_{\max}$ samples of the upchirp phase (16) when SF=12, it is possible to derive the sampled phase terms for all possible modulation symbols and all possible values of SF, with significant benefits in terms of transmitter complexity. For this reason, hereinafter we will refer to

$$\left\{ \theta^{(12)}(k) \right\}_{k=0}^{2^{13}-1} = \left\{ k\frac{\pi}{2} \left[-1 + \frac{k}{2^{13}} \right] \right\}_{k=0}^{2^{13}-1}, \tag{17}$$

as *reference upchirp phase*. Its shape is depicted in Fig.2(b).

B. Step 2: Sampled upchirp phase term for each SF

The sampled upchirp phase for all SFs (given by (16)) can be derived by properly decimating and scaling (17). More precisely, having defined the decimation factor $D = 2^{12-\mathrm{SF}}$, it is:

$$\left\{ \theta^{(\mathrm{SF})}(k) \right\}_{k=0}^{2^{\mathrm{SF}+1}-1} = \frac{1}{D} \left\{ \theta^{(12)}(Dk) \right\}_{k=0}^{2^{\mathrm{SF}+1}-1}, \tag{18}$$

The proof of (18) is reported in Appendix C.

It follows that the $2^{13} = 8192$ samples of (17) might be stored in a lookup table (LUT), so that the sampled upchirp phase for all SFs can be derived (according to (18)) by simply reading 1 sample every D in the LUT and scaling it by $\frac{1}{D}$. Alternatively, the sampled upchirp phase for a given SF might be computed run-time using (18), one sample at a time in each sampling interval T, thus avoiding the need of a LUT.

Equation (18), which refers to the sampled phase of pure upchirps, is only an intermediate step toward our final objective, which is the derivation of a similar equation expressing the sampled phase for all modulation symbols s and all SFs. Nonetheless, (18) may be directly used to generate the $\cos(\cdot)$ and $\sin(\cdot)$ terms in (12) and (13) when pure upchirps need to be transmitted, that is, in the frame preamble, and in both the payload and CRC fields when the symbol $s = 0$ (corresponding to a pure upchirp) is to be sent. Moreover, it may be used to generate also the downchirps required at the end of the preamble, by simply replacing[5] $\sin(\cdot)$ with $-\sin(\cdot)$.

Most importantly, however, (17) and (18) are the basis to generate the modulated chirps for all symbols and all SFs, as shown hereafter.

C. Step 3: Sampled phase term for each SF and each modulation symbol

The paramount importance of (17) lays in that it is the basis to generate the sampled phase $\left\{ \theta^{(\mathrm{SF})}(s, k) \right\}_{k=0}^{2^{\mathrm{SF}+1}-1}$ for all modulation symbols $s \in \mathcal{S}$ and all SFs. This is possible thanks to the following equation:

$$\left\{ \theta^{(\mathrm{SF})}\big(s, k\big) \right\} = \frac{1}{D} \left\{ \theta^{(12)}\bigg(D\big((k + 2s) \bmod 2^{\mathrm{SF}+1}\big) \bigg) \right\} \\ - \frac{1}{D}\theta^{(12)}\big(2sD\big), \tag{19}$$

---

[5]Given (14), the downchirp is obtained by simply taking $-\theta(t)$. Clearly, this impacts only on the sign of $\sin(\cdot)$, which is an odd function.
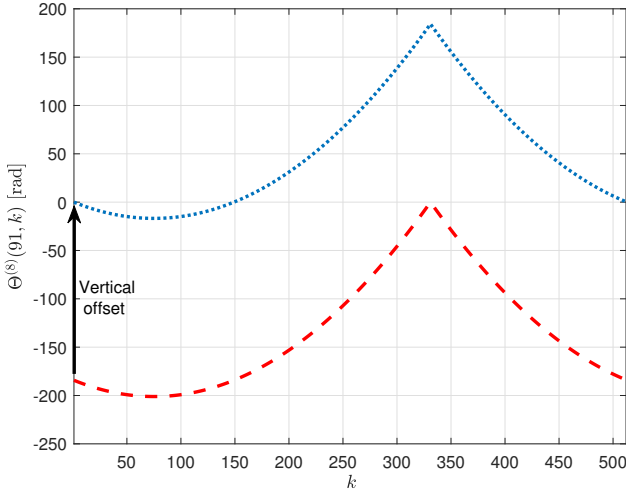
Fig. 4. Transmitter: Modulated phase with $s = 91$ and SF=8.

with $k = 0, 1, \ldots, 2^{\mathrm{SF}+1} - 1$.

The proof of (19) is reported in Appendix D.

In any symbol interval n, for any SF and modulation symbol s, (19) provides the corresponding phase samples to be fed to the $\cos(\cdot)$ and $\sin(\cdot)$ terms in (12) and (13). This results in a simple implementation of LoRa transmitters, which can thus be realized according to a digital architecture exploiting the capabilities of modern DSP microprocessors.

```
1    function [modul_phase]=phase_gen(s,SF)
2    D=2^(12-SF); % Decimation factor
3    k=0:2^13-1; %Samples index for eq.(17)
4    ref_phase=k.*pi/2.*(-1+k/2^13); % eq.(17)
5    time_adv=2*s;
6    k=1+D.*mod(time_adv+[0:1:2^(SF+1)-1],2^(SF+1));
7    modul_phase=(1/D).*ref_phase(k);
8    modul_phase=modul_phase-modul_phase(1); ...
          %Vertical offset compensation
9    end
```

Listing 1. MATLAB function for the generation of modulated phases

The MATLAB function reported in Listing 1 shows the phase generation algorithm: the function receives the modulation symbol s and the spreading factor SF as inputs, and provides the discrete-time modulated phase (19) as output. The core of the function is represented by lines 5, 6, 7 and 8, which implement (19) starting from the reference upchirp phase (17) derived in lines 3 and 4.

As an example case, the above MATLAB function has been used to derive the sampled phase depicted in Fig.4 with a dotted line-style, which refer to $s = 91$ and SF=8 (the lower curve, with a dashed line-style, is commented in Appendix D). This is the modulated phase that originates the instantaneous frequency-offset shown in Fig.1 when $B = 500$ kHz.

Remark 2. It is worth observing that the sequence of $N_{\max} = 8192$ samples provided by (17) is symmetric, meaning that $\theta^{(12)}(k) = \theta^{(12)}(2^{13} - k)$, with $k = 0, 1, \ldots, 2^{12}$ (see Appendix E for the proof). This nice property of (17), clearly evident in Fig.2(b), allows reducing by half the size of the LUT needed for its storage.

V. DEMODULATION OF LoRa SIGNALS. FREQUENCY DOMAIN INTERPRETATION

In order to investigate the basics of the demodulation method adopted by LoRa devices, let us assume that the received signal is not affected by distortion, noise and interference. This means that, with a view to providing an insight into the demodulation technique, the presence of receive filters is not considered in this section. The receiver architecture and the impact of filtering will be discussed, instead, in Sec.VI. We assume, moreover, that perfect carrier-, symbol-, and frame-synchronizations have been established, so that the receiver, after the RF to baseband conversion, exactly recovers the complex envelope (8) in each symbol interval.

As observed in [12]–[14], in the n-th symbol interval the receiver computes the twisted (dechirped) signal by multiplying the received complex envelope (8) with the complex-conjugate of a pure upchirp[6], whose phase is given in (14). In particular, in the n-th symbol interval the receiver computes:

$$r_n(t) = i_n(t)e^{-j\theta(t - nT_s)} \tag{20}$$

which results in

$$r_n(t) = \begin{cases} V_0 e^{j2\pi \frac{B}{M} s(t - nT_s)}, & nT_s \leq t < nT_s + T_{\mathrm{h}}, \\ V_0 e^{j2\pi(-B + \frac{B}{M}s)(t - nT_s)}, & nT_s + T_{\mathrm{h}} \leq t \leq (n+1)T_s. \end{cases} \tag{21}$$

Since we are considering the generic symbol interval $[nT_s, (n+1)T_s]$, the term T_{h} in (21) is the offset with respect to the beginning of the same interval. The proof of (21) is reported in Appendix F.

It clearly appears that $r_n(t)$ is a phasor with frequency

- $f_0^{(1)} = \frac{B}{M}s$ in the interval $[nT_s, nT_s + T_{\mathrm{h}}]$,
- $f_0^{(2)} = (-B + \frac{B}{M}s)$ in the interval $[nT_s + T_{\mathrm{h}}, (n+1)T_s]$.

Taking the Continuous Time Fourier Transform $R_n(f)$ of (21) and computing its modulus leads to (see Appendix G):

$$\left| R_n(f) \right| = V_0 \left| T_{\mathrm{h}} \mathrm{sinc}\left[(f - f_0^{(1)})T_{\mathrm{h}} \right] e^{-j2\pi(f - f_0^{(1)})(nT_s + \frac{T_{\mathrm{h}}}{2})} e^{-j2\pi f_0^{(1)} nT_s} \right.$$
$$\left. + T_{\widehat{\mathrm{h}}} \mathrm{sinc}\left[(f - f_0^{(2)})T_{\widehat{\mathrm{h}}} \right] e^{-j2\pi(f - f_0^{(2)})(nT_s + T_{\mathrm{h}} + \frac{T_{\widehat{\mathrm{h}}}}{2})} e^{-j2\pi f_0^{(2)} nT_s} \right| \tag{22}$$

with $T_{\widehat{\mathrm{h}}}$ denoting the residual chirp duration after the folding. It turns out that the amplitude spectrum (22) contains two $\mathrm{sinc}(\cdot)$ functions centred in $f_0^{(1)}$ and $f_0^{(2)}$, which appear as well-separated spectral lines, whose positions in the frequency axis depends on the modulation symbol s. Figure 5 shows an example of spectrum computed in the case $s = 91$, SF=8, $B = 500$ kHz (the same setting used to derive Figs.1 and 4).

Remark 3. With reference to (22), it is worth observing that

- $f_0^{(1)} \in [0, \frac{M-1}{M}B]$, whereas $f_0^{(2)} \in [-B, -B + \frac{M-1}{M}B]$, meaning that the peak of the first $\mathrm{sinc}(\cdot)$ is always in the right half-plane of the frequency domain (blue plot in Fig.5), whereas the peak of the second $\mathrm{sinc}(\cdot)$ is always in the left half-plane (red plot in Fig.5);
- the distance between the two spectral lines is B, irrespectively of the symbol s;

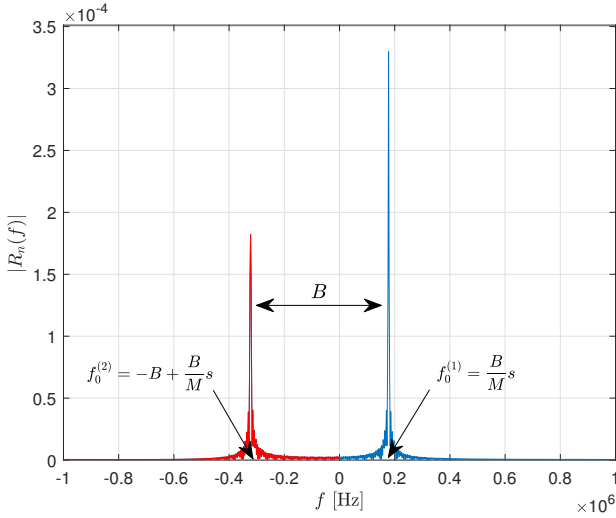[6]The complex-conjugate of a pure upchirp corresponds to a pure downchirp.

Fig. 5. Amplitude spectrum. $s = 91$, SF=8, $B = 500$ kHz.

- the spectrum (22) of the dechirped signal in a symbol interval is much more concentrated than the spectrum of the modulated signal, which spans (and exceeds) the whole $[-\frac{B}{2}, \frac{B}{2}]$ interval [14]. In fact, the dechirping results in a despreading operation, turning the distributed spectrum of (8) into two compact spectral lines;
- although more concentrated, the spectrum of the dechirped signal covers a wider frequency range than the spectrum of the modulated signal (8). In fact, depending on the symbol s, the two spectral lines might appear wherever (although with a discrete step $\frac{B}{M}$ and separated by B) in the interval $[-B, \frac{M-1}{M}B]$, whose size is almost twice that of the modulated signal spectrum.

Clearly, starting from the dechirped signal spectrum (22), it is straightforward to derive the transmitted symbol s, which is directly related to the frequency bins in which the two spectrum peaks appear. Thus, it is not surprising that the demodulation method described in the patent documents [11], [12] is based on a numerical algorithm for the detection of spectrum peaks. In particular, the demodulator described in [11], [12] works as follows:

- Step 1. It obtains the sampled version of the continuous-time dechirped signal (21) with a properly chosen sampling frequency $f_s^{(d)}$;
- Step 2. It performs the FFT of the sampled dechirped signal in each symbol time;
- Step 3. It derives the modulation symbol by detecting the bin in which the peak of the FFT modulus appears.

As pointed out earlier, however, the spectrum of the continuous-time dechirped signal has two, non-symmetric, peaks, in both the negative and positive semi-axes. So, where does the single peak mentioned by [11], [12] come from?

In this regard, the key point is the sampling frequency adopted in Step 1 for the discrete-time representation of the dechirped signal, which is suggested to be $f_s^{(d)} = B$ [11], [13], [14], [35]. It is worth noticing that, surprisingly, this choice does not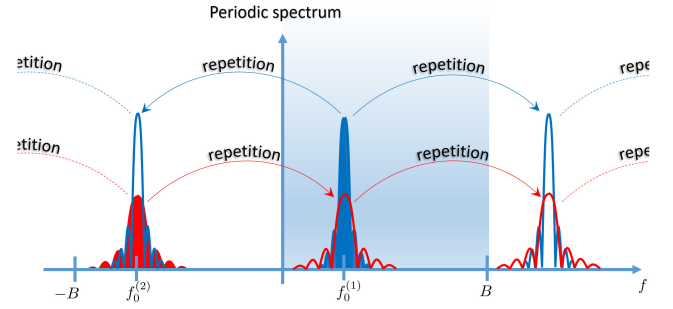 meet the sampling theorem requirement. In fact, as observed in our Remark 3, the two spectral lines of (21) fall in the frequency interval $[-B, \frac{M-1}{M}B]$, which implies that the sampling frequency should be such that $f_s^{(d)} \geq B[1 + \frac{M-1}{M}] \simeq 2B$. The straightforward consequence of the undersampling is that the sampled dechirped signal obtained in Step 1 is affected by aliasing in the frequency-domain.

More precisely, the discrete-time signal obtained sampling the dechirped signal (21) with $f_s^{(d)} = B$ has a periodic spectrum

$$R_n^{(p)}(f) = f_s^{(d)} \sum_{i=-\infty}^{\infty} R_n(f - if_s^{(d)}) \qquad (23)$$

whose period $f_s^{(d)} = B$ equals the frequency interval that separates the two spectral lines (see Fig.5), which thus overlap each other. This phenomenon is depicted in Fig.6, which shows that the periodic repetition with period B of the original spectrum (represented by color-filled contours) makes the first rightward repetition of the red spectral line exactly overlap with the blue one, and vice-versa. Clearly, the resulting spectrum (23) after Step 1 is the "coherent" sum of the overlapping components, scaled by $f_s^{(d)}$.

The FFT operation, carried out in Step 2 of the demodulation procedure, provides the receiver with a sampled representation of (23) in the frequency interval $[0, B]$, which is highlighted in Fig.6 by means of the coloured background box. It is evident, now, that the spectral line that appears in such interval arises as the superposition (i.e., aliasing) of the two spectral lines of the continuous-time dechirped signal (21).

In Step 3 of the demodulation procedure, given the relation $f_0^{(1)} = \frac{B}{M}s$, it is straightforward for the demodulator to derive the transmitted symbol s by locating the frequency bin in which the peak of this spectral line falls.

As far as the value $A = |R_n^{(p)}(f_0^{(1)})|$ of the useful peak is concerned, in Appendix H we show that it is an increasing function of SF through the following simple equation:

$$A = V_0 2^{\text{SF}}. \qquad (24)$$

Equation (24) shows under a new perspective why higher SFs provide better performance in terms of communication reliability. What's more, (24) shows that A scales exponentially with SF.

Remark 4. The overlapping of the two spectral components due to the undersampling of (21) is extremely beneficial for
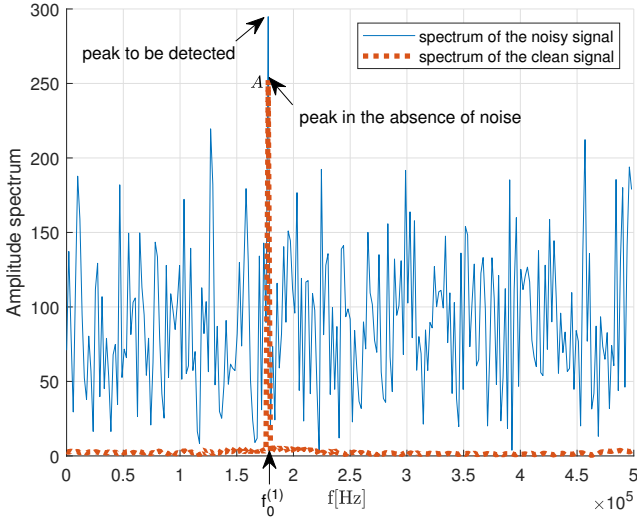

Fig. 6. Periodic repetition of the original spectrum with aliasing.

Fig. 7. Amplitude spectrum of the sampled dechirped signal. SF=8, $B = 500$kHz, $s = 91$, $V_0 = 1$, $A = 256$, $\frac{E_s}{N_0} = 8$ dB.

Fig. 8. Direct-conversion receiver. PA=power amplifier, LP=low-pass, ADC=analog-to-digital converter.

the demodulator, as the amplitude of the resulting spectral line is higher than those of the two original ones. Clearly, this increases the probability that its peak is detected even in the presence of noise and interference.

This aspect can be clearly appreciated observing Fig.7, which shows the FFT modulus of the discrete-time dechirped signal (that is, the input of Step 3), both in the presence and in the absence of AWGN noise, when $s = 91$, SF=8 and $B = 500$ kHz. The noise-impaired spectrum refers, in particular, to the case $\frac{E_s}{N_0} = 8$ dB, with E_s denoting the energy of the received chirp and N_0 representing the single-sided power spectrum of the noise.

One observes the existence of significant unwanted spectral peaks originated by the additive noise (which underwent the dechirping as well), that might mislead the receiver. By chance, in the specific case depicted in Fig.7 the noise also increased the useful spectrum peak, thus mitigating its detrimental impact.

Figure 7 also shows that the peak of the uncorrupted spectral line is $A = 256$, which is the expected value, following (24), as it has been obtained implementing the demodulation procedure with MATLAB in the case $V_0 = 1$ and SF=8.

VI. BASEBAND DIGITAL FILTER DESIGN

Modern receivers are implemented combining analog and digital signal processing: the former takes place in the RF stage and, if any, in the intermediate frequency (IF) stage, whereas numerical techniques are adopted in the baseband stage, where signals are represented through their sampled versions obtained by means of analog-to-digital converters (ADCs).

In this regard, Fig.8 shows the architecture of a direct-conversion (also called zero-IF or homodyne) receiver, which converts the RF analog signal directly to the baseband, thus deriving the in-phase and quadrature components $p^{(r)}(t)$ and $q^{(r)}(t)$ of the received signal in a single down-conversion step. The superheterodyne architecture, where RF signals are
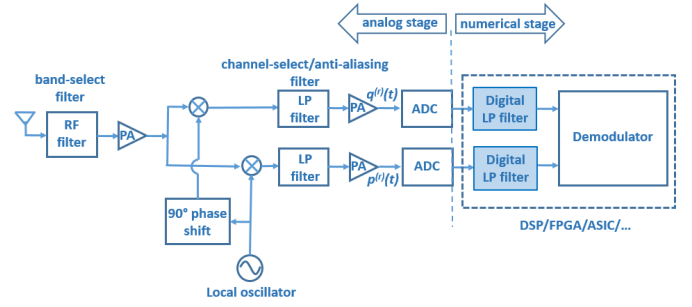
down-converted to the baseband after a preliminary conversion to IF, is the well-known and widely adopted alternative, although direct conversion has obvious advantages in terms of power consumption, cost and hardware dimension, which are fundamental aspects for the LoRa technology.

Irrespectively of the architecture adopted to derive $p^{(r)}(t)$ and $q^{(r)}(t)$, either homodyne or superheterodyne, such baseband signals are then sampled by ADCs, whose outputs are then provided to a digital signal processing unit, such as a DSP, an FPGA or an ASIC, where numerical techniques are implemented to complete the demodulation process.

Taking as a reference the direct-conversion receiver shown in Fig.8, in this section we focus our attention on the low pass (LP) digital filters implemented in the numerical stage, which are highlighted as coloured blocks in the figure. The same digital filters are however implemented also in the baseband stage of superheterodyne receivers, which makes the following discussion absolutely general.

Before going into the details of our analysis, let us recall the different objectives of the analog and digital filters shown in Fig.8, which is instrumental to the clarity of our discussion. The analog filters are in charge of removing out-of-band RF interferers ($\rightarrow$ the RF analog filter) as well as selecting the useful channel ($\rightarrow$ the LP analog filters), also removing the noise and avoiding the occurrence of spectral aliasing with adjacent channels after the analog-to-digital conversion.

Considering the fact that the baseband stage of a LoRa receiver is certainly equipped with a digital signal processing unit, which is in charge of the FFT operation required for the demodulation, LP digital filters can be easily implemented as well (see the coloured blocks in Fig.8) with no additional hardware complexity, having the specific purpose of reducing as much as possible the noise contribution. This is extremely beneficial, as it allows to design the analog RF and LP filters with the only purpose of removing the adjacent channel interferers, which are at least one guard-band apart. It follows that, thanks to the presence of the LP digital filters, less frequency-selective (therefore, less complicated from a circuital point of view) analog RF and LP filters can be implemented.

Clearly, the counterpart is that the LP digital filters, in charge of removing the out-of-band noise, must be very selective, resembling as much as possible to ideal filters, that is, non-distorting filters with a pass-band equal to the bandwidth $\frac{B_{99}}{2} \simeq \frac{B}{2}$ of the baseband signals $p^{(r)}(t)$ and
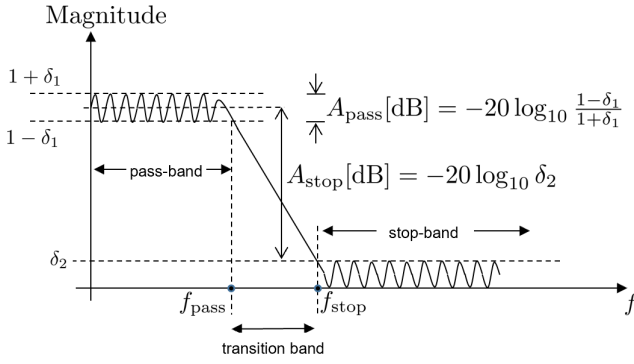
This article has been accepted for publication in IEEE Transactions on Wireless Communications. This is the author's version which has not been fully edited and content may change prior to final publication. Citation information: DOI 10.1109/TWC.2021.3095667

IEEE TRANSACTIONS ON WIRELESS COMMUNICATIONS, VOL. XX, NO. Y, MONTH 20XX
9

Fig. 9.   Filter design mask.

Fig. 10.   Symbol error rate. $B = 125$ kHz, f_{pass}=62.5 kHz.

$q^{(r)}(t)$. As it turns out, the reduced circuital complexity of analog filters is traded with the increased complexity of the software implementation of digital filters.

As it is known, non-distorting digital filters can be implemented using finite impulse response (FIR) design techniques, with a selectivity that improves as the number of filter coefficients increases. Improving the selectivity, which has a beneficial impact on the receiver performance, has, however, two major drawbacks:

- an increased computational power (that is, a more powerful hardware) may be required, as the number of multiplications and sums carried out in the unit time by the two digital filters increases with the number of coefficients,
- an increased energy consumption, due to the augmented computational effort.

Both issues are quite critical for LoRa end nodes, which are required to cost only a few dollars and last for many years. Therefore, the receiver design should be carried out considering the relation between the receiver performance and the number of filter coefficients, which is the focus of this section.

We addressed this topic by implementing a MATLAB simulator of a complete LoRa transceiver (transmitter + receiver) working in an AWGN channel. At the receiver side, in particular, we implemented the two linear-phase LP FIR filters depicted in Fig.8, whose characteristics, namely,

- the pass-band width f_{pass},
- the pass-band ripple A_{pass},
- the lower stop-band edge f_{stop},
- the stop-band attenuation A_{stop},

have been properly tuned, as discussed in the following. The reader is referred to Fig.9 for an explicative, pictorial representation of the above mentioned parameters.

As a first step, we validated the simulator by retrieving the results reported in [15] and [16], which refer to the symbol error rate (i.e., the chirp error rate) as a function of the signal-to-noise ratio SNR $= \frac{P_s}{P_w}$, where

- P_s denotes the average signal power,
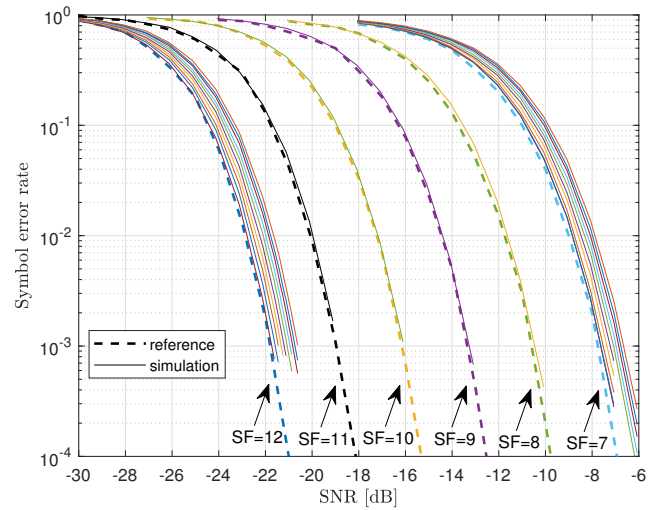- $P_w = N_0 B$ denotes the noise power within the nominal signal bandwidth B.

Such reference performance curves, obtained assuming ideal receive filters with a pass-band equal to the nominal signal bandwidth, are plotted in Fig.10 with a dashed line-style. Considering LoRa signals with $B = 125$kHz, the same curves were obtained with our simulator by adopting the following settings for the two LP digital filters:

- $f_{pass} = \frac{B}{2} = 62.5$ kHz, which is coincident with the nominal bandwidth of the baseband signals $p^{(r)}(t)$ and $q^{(r)}(t)$ at the filters' input ports,
- $A_{pass} = 0.01$ dB, which means that the amplitude distortion introduced by the filters' ripple within the pass-band is practically negligible,
- $f_{stop} = 64$ kHz, which corresponds to very selective filters, as the width of the transition band is only 1.5 kHz. This is consistent with the attempt to approximate the ideal filters considered in [15], [16],
- $A_{stop} = 30$dB, which appears reasonable for practical filters. Clearly, given the hypothesis of ideal filters, [15], [16] assume $A_{stop} = +\infty$,
- $f_s^{(ADC)} = 250\frac{\text{ksamples}}{\text{s}}$, with $f_s^{(ADC)}$ denoting the sampling frequency adopted by the ADCs, which represents the filters' clock.

As shown in Fig.10, when such filters (each requiring 409 coefficients) are implemented in the LoRa simulator, the resulting symbol error rates are almost coincident with the reference ones for each SF. This is immediately evident in Fig.10 for SF=8, 9, 10 and 11, for which only the reference and the simulated curves are reported. As far as the cases SF=7 and SF=12 are concerned, the practical coincidence between the reference curves and the simulated ones is also true, although less evident in Fig.10, which shows bunches of curves related to the experienced symbol error rates also for less selective filters, with f_{stop}=64kHz, 68kHz, 72kHz, ..., 98kHz.

In particular, still assuming $f_{pass} = 62.5$ kHz, $A_{pass} = 0.01$ dB and $A_{stop} = 30$ dB, the two bunches of curves for SF=7 and SF=12 highlight the performance degradation that is to be expected passing from f_{stop}=64 kHz (leftmost simulated curve of each bunch) to f_{stop}=98 kHz

f_{stop}	Number of coefficients	SF=7 SNR @ 10^{-3}	SF=12 SNR @ 10^{-3}
64kHz	409	-21.73 dB	-7.64 dB
68kHz	113	-21.58 dB	-7.62 dB
72kHz	65	-21.45 dB	-7.53 dB
76kHz	47	-21.33 dB	-7.37 dB
80kHz	37	-21.20 dB	-7.22 dB
84kHz	29	-21.07 dB	-7.15 dB
86kHz	25	-20.95 dB	-7.03 dB
90kHz	21	-20.83 dB	-6.92 dB
94kHz	19	-20.74 dB	-6.81 dB
98kHz	17	-20.61 dB	-6.70 dB

TABLE II
TRADE-OFF BETWEEN FILTER SELECTIVITY AND RECEIVER PERFORMANCE.

(rightmost simulated curve of each bunch), which corresponds, for both SF=7 and SF=12, to an SNR loss of about 1dB for a target symbol error rate of 10^{-3}. On the other hand, as shown in Table II, the benefit in terms of number of coefficients required to implement each of the two filters is quite relevant, as it passes from 409 for f_{stop}=64 kHz to only 17 for f_{stop}=98 kHz.

Clearly, intermediate choices are possible, which are presented in Table II. For instance, passing from f_{stop}=64 kHz to f_{stop}=68 kHz allows saving nearly 300 coefficients for each filter with an almost insignificant SNR loss for the target symbol error rate 10^{-3}.

Comments on $f_s^{(ADC)}$ and $f^{(d)}$. In this section, we assumed that the sampling frequency $f_s^{(ADC)}$ adopted by the ADCs fully meets the Shannon-Hartley sampling theorem. This is a mandatory condition to design digital filters capable of preserving the useful signal while reducing the out-of-band noise. However, in Sec.V we pointed out that the sampling frequency $f^{(d)} = B$, which purposely does not meet the sampling theorem requirement, must be adopted in the demodulation process (Sec.V, Step 1). This means that the demodulator must include a downsampling stage, which reduces the sampling frequency from $f_s^{(ADC)}$ to $f^{(d)} = B$ immediately after the filters.

In order to keep the downsampler as simple as possible, it is convenient to choose $f_s^{(ADC)}$ as an integer multiple of $f^{(d)}$, that is, $f_s^{(ADC)} = Lf^{(d)} = LB$, with $L \in \mathbb{Z}$ and $L > 1$. In such a case, the downsampler needs only to select one sample every L. In the numerical results, given the choice $f_s^{(ADC)} = 250\frac{\text{ksamples}}{\text{s}}$ for the considered LoRa signals with $B = 125$ kHz, we assumed $L = 2$.

VII. CONCLUSIONS

In this paper, we analytically investigated the generation and the demodulation of LoRa signals, as well as the trade-off between the receiver performance and the number of coefficients of the receive digital filters. We firstly provided a simple algorithm for the numerical computation of the signal samples at the transmitter side. Then, we showed that the effectiveness of the demodulation technique depends on the fact that the

sampling frequency at the receiver is forced to violate the sampling theorem requirement. Finally, we showed that the number of coefficients of the digital filters implemented in the baseband stage of the receiver might be significantly reduced, at the cost of an almost negligible increase of the signal-to-noise ratio required for a given performance level.

APPENDIX A
PROOF OF (6)

Proof: Given (4), it follows that

$$\theta(s, T_s) = 2\pi \int_0^{T_s} \Delta f(s, \xi) d\xi = 0.$$

Being, of course,

$$\theta(s, 0) = 2\pi \int_0^0 \Delta f(s, \xi) d\xi = 0$$

the proof of (6) is immediately obtained. ∎

APPENDIX B
PROOF OF (16)

Proof: Given (14) and (15), it is:

$$\left\{\theta(k)\right\}_{k=0}^{N-1} = \left\{\pi B\left[-kT + \frac{k^2 T^2}{T_s}\right]\right\}_{k=0}^{N-1}.$$

Having assumed $f_s = 2B$, one obtains $T = \frac{1}{2B}$ and therefore:

$$\left\{\theta(k)\right\}_{k=0}^{N-1} = \left\{\pi B\left[-\frac{k}{2B} + \frac{k^2}{4B^2 T_s}\right]\right\}_{k=0}^{N-1}$$
$$= \left\{k\frac{\pi}{2}\left[-1 + \frac{k}{2BT_s}\right]\right\}_{k=0}^{N-1}.$$

Since $BT_s = M = 2^{\text{SF}}$, and explicitly showing the dependence on SF, (16) is immediately derived. ∎

APPENDIX C
PROOF OF (18)

Proof: Given the reference sampled phase (17), one considers its decimated version, obtained taking 1 sample every $D = 2^{12-\text{SF}}$ samples. It results

$$\left\{\theta^{(12)}(Dk)\right\}_{k=0}^{\frac{2^{13}}{D}-1} = \left\{Dk\frac{\pi}{2}\left[-1 + \frac{Dk}{2^{13}}\right]\right\}_{k=0}^{\frac{2^{13}}{D}-1}.$$

Observing that $\frac{2^{13}}{D} = 2^{\text{SF}+1}$, one obtains

$$\left\{\theta^{(12)}(Dk)\right\}_{k=0}^{2^{\text{SF}+1}-1} = D\left\{k\frac{\pi}{2}\left[-1 + \frac{k}{2^{\text{SF}+1}}\right]\right\}_{k=0}^{2^{\text{SF}+1}-1}.$$

Recalling (16) it follows

$$\left\{\theta^{(12)}(Dk)\right\}_{k=0}^{2^{\text{SF}+1}-1} = D\left\{\theta^{(\text{SF})}(k)\right\}_{k=0}^{2^{\text{SF}+1}-1},$$

and, ultimately

$$\left\{\theta^{(\text{SF})}(k)\right\}_{k=0}^{2^{\text{SF}+1}-1} = \frac{1}{D}\left\{\theta^{(12)}(Dk)\right\}_{k=0}^{2^{\text{SF}+1}-1}.$$

∎

$$\theta(s^{(n)}, t) = \begin{cases} 2\pi[-\frac{B}{2}(t - nT_s) + \frac{B}{M}s(t - nT_s) + \frac{B}{2T_s}(t - nT_s)^2], \ nT_s \le t < nT_s + T_\mathrm{h}, \\ 2\pi[-\frac{3B}{2}(t - nT_s) + \frac{B}{M}s(t - nT_s) + \frac{B}{2T_s}(t - nT_s)^2], \ nT_s + T_\mathrm{h} \le t \le (n + 1)T_s. \end{cases} \quad (28)$$

APPENDIX D
PROOF OF (19)

Proof: For a given SF, (16) provides the (sampled) phase term of a pure upchirp, whose instantaneous frequency-offset sweeps the entire interval $[-\frac{B}{2}, \frac{B}{2}]$ starting from its lowest boundary $-\frac{B}{2}$ (see Fig.2(a)). A chirp modulated by a symbol s is different from a pure upchirp in that its instantaneous frequency-offset sweeps the same interval starting from a higher value, given by $-\frac{B}{2} + \frac{B}{M}s$, then it wraps around to $-\frac{B}{2}$ as soon as it reaches $\frac{B}{2}$ and keeps on increasing until the end of the symbol interval (see Fig.1).

Considering the reference symbol interval $[0, T_s]$, the instantaneous frequency-offset of a chirp modulated by a symbol s can thus be considered as the result of a time advance (that is, a left shift along the time axis), whose entity depends on s, of the instantaneous frequency-offset of a pure upchirp. This modelling is complete on condition that the symbol time interval is given the circularity property, so that the translated instantaneous frequency-offset wraps around "horizontally" in $t = 0$, making it enter from the right boundary of the symbol interval what exits from the left boundary.

In particular, starting from the phase term (16) of a pure upchirp, a new phase term can be derived as follows, which provides the frequency sweep associated to a certain modulation symbol s:

$$\left\{ \theta^{(\mathrm{SF})}\Big((k + 2s) \bmod 2^{\mathrm{SF}+1} \Big) \right\}_{k=0}^{2^{\mathrm{SF}+1}-1}. \quad (25)$$

Equation (25) incorporates both the time advance, given by $2s$, and the wrap-around feature, given by the $\bmod$ operation. One observes, in particular, that since the number of modulation symbols is M, whereas the number of samples in a chirp interval is $2M$ (see, Sec.IV-A), the number of samples corresponding to a time advance of s is $2s$.

Although (25) provides the right frequency sweep for any given symbol s, it lacks of the fundamental property of null phase at the boundaries of symbol intervals (*Property 1*, Sec.III). This is clearly evident in Fig.4, where the dashed curve represents the phase term given by (25) in the case $s = 91$ and SF=8.

The null phase at the boundaries of the symbol interval can be simply obtained by compensating (i.e., removing) the vertical offset $\theta^{(\mathrm{SF})}(2s)$ exhibited by (25) for $k = 0$ (see Fig.4), thus obtaining:

$$\left\{ \theta^{(\mathrm{SF})}\Big(s, k \Big) \right\} = \left\{ \theta^{(\mathrm{SF})}\Big((k + 2s) \bmod 2^{\mathrm{SF}+1} \Big) \right\} - \theta^{(\mathrm{SF})}\Big(2s \Big) \quad (26)$$

with $k = 0, 1, \ldots, 2^{\mathrm{SF}+1} - 1$. In the example case $s = 91$ and SF=8, the resulting phase term is shown in Fig.4 with a dotted line-style. One observes, by the way, that both phases shown in Fig.4 provide the right frequency sweep, which is the one depicted in Fig.1. Nonetheless, the dashed curve is not compliant with the LoRa specifications.

Plugging (18) in (26), it finally results:

$$\left\{ \theta^{(\mathrm{SF})}\Big(s, k \Big) \right\} = \frac{1}{D} \left\{ \theta^{(12)}\Big(D\Big((k + 2s) \bmod 2^{\mathrm{SF}+1} \Big) \Big) \right\} - \frac{1}{D}\theta^{(12)}\Big(2sD \Big),$$

with $k = 0, 1, \ldots, 2^{\mathrm{SF}+1} - 1$. ∎

APPENDIX E
SYMMETRY OF THE REFERENCE UPCHIRP PHASE

It must be proved that $\theta^{(12)}(2^{13} - k) = \theta^{(12)}(k)$ with $k = 0, 1, \ldots, 2^{12}$.

Proof: Starting from (17) it is

$$\theta^{(12)}(2^{13} - k) = (2^{13} - k)\frac{\pi}{2}\left[-1 + \frac{2^{13} - k}{2^{13}} \right].$$

After easy manipulations of the right-hand term, one obtains:

$$\theta^{(12)}(2^{13} - k) = \frac{\pi}{2}k\Big(-1 + \frac{k}{2^{13}} \Big)$$

Recalling (17) it immediately follows:

$$\theta^{(12)}(2^{13} - k) = \theta^{(12)}(k).$$

Clearly, both terms of the above equality are sound only provided that their arguments are meaningful, which means $0 \le k \le 2^{13}$. Such interval includes the range $k = 0, 1, \ldots, 2^{12}$ of interest for this proof. ∎

APPENDIX F
PROOF OF (21)

Proof: Given (8), in the n-th symbol interval $[nT_s, (n + 1)T_s]$ the receiver obtains:

$$\begin{aligned} r_n(t) &= i_n(t)e^{-j\theta(t - nT_s)} \\ &= V_0 e^{j\theta(s^{(n)}, t)}e^{-j\theta(t - nT_s)}, \end{aligned} \quad (27)$$

where $\theta(s^{(n)}, t)$ can be easily derived from (3) as in (28).

Plugging (28) and (14) in (27) immediately leads to (21). ∎

APPENDIX G
PROOF OF (22)

Proof: Equation (21) can be rewritten as

$$\begin{aligned} r_n(t) &= V_0 e^{j2\pi f_0^{(1)}(t - nT_s)}g_{T_\mathrm{h}}(t - nT_s) \\ &+ V_0 e^{j2\pi f_0^{(2)}(t - nT_s)}g_{T_\mathrm{\bar{h}}}(t - nT_s - T_\mathrm{h}). \end{aligned} \quad (29)$$

Taking the continuous Fourier transform and denoting with * the linear convolution, (30) is immediately obtained, with $\delta(\cdot)$ denoting the Dirac's delta. ∎

$$R_n(f) = \left(V_0\delta(f - f_0^{(1)})e^{-j2\pi f nT_s}\right) * \left(T_{\mathrm{h}}\mathrm{sinc}(fT_{\mathrm{h}})e^{-j2\pi f(nT_s+\frac{T_{\mathrm{h}}}{2})}\right)$$
$$+ \left(V_0\delta(f - f_0^{(2)})e^{-j2\pi f nT_s}\right) * \left(T_{\widehat{\mathrm{h}}}\mathrm{sinc}(fT_{\widehat{\mathrm{h}}})e^{-j2\pi f(nT_s+T_{\mathrm{h}}+\frac{T_{\widehat{\mathrm{h}}}}{2})}\right)$$
$$= V_0 T_{\mathrm{h}}\mathrm{sinc}\left[(f - f_0^{(1)})T_{\mathrm{h}}\right]e^{-j2\pi(f-f_0^{(1)})(nT_s+\frac{T_{\mathrm{h}}}{2})}e^{-j2\pi f_0^{(1)}nT_s}$$
$$+ V_0 T_{\widehat{\mathrm{h}}}\mathrm{sinc}\left[(f - f_0^{(2)})T_{\widehat{\mathrm{h}}}\right]e^{-j2\pi(f-f_0^{(2)})(nT_s+T_{\mathrm{h}}+\frac{T_{\widehat{\mathrm{h}}}}{2})}e^{-j2\pi f_0^{(2)}nT_s}. \tag{30}$$

$$R_n^{(p)}(f) = V_0 B\Big[T_{\mathrm{h}}\mathrm{sinc}[(f - f_0^{(1)})T_{\mathrm{h}}]e^{-j2\pi(f-f_0^{(1)})(nT_s+\frac{T_{\mathrm{h}}}{2})}e^{-j2\pi f_0^{(1)}nT_s}$$
$$+ T_{\widehat{\mathrm{h}}}\mathrm{sinc}[(f - f_0^{(2)} - B)T_{\widehat{\mathrm{h}}}]e^{-j2\pi(f-f_0^{(2)}-B)(nT_s+T_{\mathrm{h}}+\frac{T_{\widehat{\mathrm{h}}}}{2})}e^{-j2\pi f_0^{(2)}nT_s}\Big]. \tag{33}$$

$$R_n^{(p)}(f) = V_0 B\Big[T_{\mathrm{h}}\mathrm{sinc}[(f - f_0^{(1)})T_{\mathrm{h}}]e^{-j2\pi(f-f_0^{(1)})(nT_s+\frac{T_{\mathrm{h}}}{2})}e^{-j2\pi f_0^{(1)}nT_s}$$
$$+ T_{\widehat{\mathrm{h}}}\mathrm{sinc}[(f - f_0^{(1)})T_{\widehat{\mathrm{h}}}]e^{-j2\pi(f-f_0^{(1)})(nT_s+T_{\mathrm{h}}+\frac{T_{\widehat{\mathrm{h}}}}{2})}e^{-j2\pi f_0^{(2)}nT_s}\Big]. \tag{34}$$

APPENDIX H
PROOF OF (24)

Proof: In Appendix G we showed that the spectral component of (22) centred in $f_0^{(1)}$ arises from the term

$$V_0 T_{\mathrm{h}}\mathrm{sinc}\left[(f - f_0^{(1)})T_{\mathrm{h}}\right]e^{-j2\pi(f-f_0^{(1)})(nT_s+\frac{T_{\mathrm{h}}}{2})}e^{-j2\pi f_0^{(1)}nT_s} \tag{31}$$

whereas the spectral component centred in $f_0^{(2)}$ arises from the term

$$V_0 T_{\widehat{\mathrm{h}}}\mathrm{sinc}\left[(f - f_0^{(2)})T_{\widehat{\mathrm{h}}}\right]e^{-j2\pi(f-f_0^{(2)})(nT_s+T_{\mathrm{h}}+\frac{T_{\widehat{\mathrm{h}}}}{2})}e^{-j2\pi f_0^{(2)}nT_s}. \tag{32}$$

Recalling (23) and focusing the attention on the frequency interval $[0, B]$, we observe that, owing to the undersampling, (32) is periodically repeated with period B and overlaps with (31) around $f_0^{(1)}$, generating the spectral component given by (33) for $f \in [0, B]$. Observing that $f_0^{(2)} + B = f_0^{(1)}$, (34) is immediately derived.

Finally, computing the value of (34) for $f = f_0^{(1)}$ gives

$$R_n^{(p)}(f_0^{(1)}) = V_0 B\Big[T_{\mathrm{h}}e^{-j2\pi f_0^{(1)}nT_s} + T_{\widehat{\mathrm{h}}}e^{-j2\pi f_0^{(2)}nT_s}\Big]$$
$$= V_0 B\Big[T_{\mathrm{h}}e^{-j2\pi f_0^{(1)}nT_s} + T_{\widehat{\mathrm{h}}}e^{-j2\pi(f_0^{(1)}-B)nT_s}\Big]$$
$$= V_0 B\Big[T_{\mathrm{h}}e^{-j2\pi f_0^{(1)}nT_s} + T_{\widehat{\mathrm{h}}}e^{-j2\pi f_0^{(1)}nT_s}e^{j2\pi BnT_s}\Big]$$
$$= V_0 B\Big[T_{\mathrm{h}}e^{-j2\pi f_0^{(1)}nT_s} + T_{\widehat{\mathrm{h}}}e^{-j2\pi f_0^{(1)}nT_s}e^{j2\pi Mn}\Big]$$
$$= V_0 B\Big[T_{\mathrm{h}} + T_{\widehat{\mathrm{h}}}\Big]e^{-j2\pi f_0^{(1)}nT_s}$$
$$= V_0 B T_s e^{-j2\pi f_0^{(1)}nT_s}$$
$$= V_0 2^{\mathrm{SF}}e^{-j2\pi f_0^{(1)}nT_s}. \tag{35}$$

Taking the modulus of (35) leads to (24). ∎

ACKNOWLEDGMENT

The author is in debt with Prof. Marco Chiani for his inspiring paper [14] and for the fruitful and encouraging discussions on LoRa. The author is also deeply grateful to Prof. Oreste Andrisano for helpful suggestions.

REFERENCES

[1] K. Ashton, "That 'Internet of Things' Thing," https://www.rfidjournal.com/that-internet-of-things-thing, 2009, [Online; accessed 06-July-2021].

[2] U. Raza, P. Kulkarni, and M. Sooriyabandara, "Low power wide area networks: An overview," *IEEE Communications Surveys Tutorials*, vol. 19, no. 2, pp. 855–873, 2017.

[3] K. Mekki, E. Bajic, F. Chaxel, and F. Meyer, "Overview of cellular LPWAN technologies for IoT deployment: Sigfox, LoRaWAN, and NB-IoT," in *IEEE International Conference on Pervasive Computing and Communications Workshops (PerCom Workshops)*, 2018, pp. 197–202.

[4] "LoRa Alliance," https://lora-alliance.org/, 2020, [Online; accessed 06-July-2021].

[5] O. Khutsoane, B. Isong, and A. M. Abu-Mahfouz, "IoT devices and applications based on LoRa/LoRaWAN," in *43rd Annual Conference of the IEEE Industrial Electronics Society (IECON)*, 2017, pp. 6107–6112.

[6] J. Haxhibeqiri, E. De Poorter, I. Moerman, and J. Hoebeke, "A survey of LoRaWAN for IoT: From technology to application," *Sensors*, vol. 18, no. 11, 2018.

[7] G. Pasolini, C. Buratti, L. Feltrin, F. Zabini, R. Verdone, O. Andrisano, and C. De Castro, "Smart city pilot project using LoRa," in *European Wireless 2018; 24th European Wireless Conference*, 2018, pp. 1–6.

[8] G. Pasolini, C. Buratti, L. Feltrin, F. Zabini, C. De Castro, R. Verdone, and O. Andrisano, "Smart city pilot projects using LoRa and IEEE802.15.4 technologies," *Sensors*, vol. 18, no. 4, 2018.

[9] "Semtech Corporation," https://www.semtech.com/lora, 2020, [Online; accessed 06-July-2021].

[10] "LoRaWAN Specifications," https://lora-alliance.org/resource-hub/lorawanr-specification-v103, 2020, [Online; accessed 06-July-2021].

[11] "EP2763321A1," https://patents.google.com/patent/EP2763321A1, 2020, [Online; accessed 06-July-2021].

[12] "EP2449690B1," https://patents.google.com/patent/EP2449690B1/en, 2020, [Online; accessed 06-July-2021].

[13] L. Vangelista, "Frequency shift chirp modulation: The LoRa modulation," *IEEE Signal Processing Letters*, vol. 24, no. 12, pp. 1818–1821, Dec 2017.

[14] M. Chiani and A. Elzanaty, "On the LoRa modulation for IoT: Waveform properties and spectral analysis," *IEEE Internet of Things Journal*, vol. 6, no. 5, pp. 8463–8470, Oct 2019.

[15] O. Afisiadis, M. Cotting, A. Burg, and A. Balatsoukas-Stimming, "On the error rate of the LoRa modulation with interference," *IEEE Transactions on Wireless Communications*, vol. 19, no. 2, pp. 1292–1304, 2020.

[16] G. Ferré and A. Giremus, "LoRa physical layer principle and performance analysis," in *25th IEEE International Conference on Electronics, Circuits and Systems (ICECS)*, 2018, pp. 65–68.

[17] T. Elshabrawy and J. Robert, "Closed-form approximation of LoRa modulation BER performance," *IEEE Communications Letters*, vol. 22, no. 9, pp. 1778–1781, 2018.

[18] H. Mroue, A. Nasser, B. Parrein, S. Hamrioui, E. Mona-Cruz, and G. Rouyer, "Analytical and simulation study for LoRa modulation," in *25th International Conference on Telecommunications (ICT)*, 2018, pp. 655–659.

[19] A. Marquet, N. Montavont, and G. Z. Papadopoulos, "Investigating theoretical performance and demodulation techniques for LoRa," in *IEEE 20th International Symposium on "A World of Wireless, Mobile and Multimedia Networks" (WoWMoM)*, 2019, pp. 1–6.

[20] T. T. Nguyen, H. H. Nguyen, R. Barton, and P. Grossetete, "Efficient design of chirp spread spectrum modulation for low-power wide-area networks," *IEEE Internet of Things Journal*, vol. 6, no. 6, pp. 9503–9515, 2019.

[21] T. Elshabrawy and J. Robert, "Interleaved chirp spreading LoRa-based modulation," *IEEE Internet of Things Journal*, vol. 6, no. 2, pp. 3855–3863, 2019.

[22] T. Elshabrawy, P. Edward, M. Ashour, and J. Robert, "On the different mathematical realizations for the digital synthesis of LoRa-based modulation," in *European Wireless 2019; 25th European Wireless Conference*, 2019, pp. 1–6.

[23] A. Thomas and N. V. Eldhose, "Performance evaluation of chirp spread spectrum as used in lora physical layer," in *IEEE International Conference on System, Computation, Automation and Networking (ICSCAN)*, 2019, pp. 1–6.

[24] B. Dunlop, H. H. Nguyen, R. Barton, and J. Henry, "Interference analysis for LoRa chirp spread spectrum signals," in *IEEE Canadian Conference of Electrical and Computer Engineering (CCECE)*, 2019, pp. 1–5.

[25] J. M. de Souza Sant'Ana, A. Hoeller, R. D. Souza, H. Alves, and S. Montejo-Sánchez, "LoRa performance analysis with superposed signal decoding," *IEEE Wireless Communications Letters*, vol. 9, no. 11, pp. 1865–1868, 2020.

[26] U. Noreen, L. Clavier, and A. Bounceur, "LoRa-like CSS-based PHY layer, capture effect and serial interference cancellation," in *24th European Wireless Conference*, 2018, pp. 1–6.

[27] P. Edward, A. Muhammad, S. Elzeiny, M. Ashour, T. Elshabrawy, and J. Robert, "Enhancing the capture capabilities of LoRa receivers," in *International Conference on Smart Applications, Communications and Networking (SmartNets)*, 2019, pp. 1–6.

[28] C. Phamand M. Ehsan, "Dense deployment of LoRa networks: Expectations and limits of channel activity detection and capture effect for radio channel access," *Sensors*, vol. 21, no. 3, 2021.

[29] R. B. Sorensen, N. Razmi, J. J. Nielsen, and P. Popovski, "Analysis of LoRaWAN uplink with multiple demodulating paths and capture effect," in *IEEE International Conference on Communications (ICC)*, 2019, pp. 1–6.

[30] D. Bankov, E. Khorov, and A. Lyakhov, "Mathematical model of LoRaWAN channel access with capture effect," in *IEEE 28th Annual International Symposium on Personal, Indoor, and Mobile Radio Communications (PIMRC)*, 2017, pp. 1–5.

[31] C. Pham, A. Bounceur, L. Clavier, U. Noreen, and M. Ehsan, "Investigating and experimenting interference mitigation by capture effect in LoRa networks," in *3rd International Conference on Future Networks and Distributed Systems*, New York, NY, USA, 2019, ICFNDS '19, Association for Computing Machinery.

[32] "Semtech Corporation. AN1200.22 LoRa Modulation Basics, May 2015," http://wiki.lahoud.fr/lib/exe/fetch.php?media=an1200.22.pdf, 2020, [Online; accessed 06-July-2021].

[33] A. Augustin, J. Yi, T. Clausen, and W. M. Townsley, "A study of LoRa: Long range & low power networks for the Internet of Things," *Sensors*, vol. 16, no. 9, 2016.

[34] N. Sornin and A.Yegin, "LoRaWAN specification," https://lora-alliance.org/wp-content/uploads/2020/11/lorawantm_specification_-v1.1.pdf, 2017, [Online; accessed 06-July-2021].

[35] R. Ghanaatian, O. Afisiadis, M. Cotting, and A. Burg, "LoRa digital receiver analysis and implementation," in *IEEE International Conference on Acoustics, Speech and Signal Processing (ICASSP)*, 2019, pp. 1498–1502.